IIETA International Information and Engineering Technology Association
Advancing the World of Information and Engineering

Journal Européen des Systèmes Automatisés
Vol. 59, No. 6, June, 2026, pp. 1665-1673
Journal homepage: http://iieta.org/journals/jesa

Robust Cascaded Synergetic Speed Control with Closed-Form Predictive Current Loop for Permanent Magnet Synchronous Motor Drives

Houcine Sayaf[1*], Katia Kouzi[1], Islam Benhamida[2], Abdelhak Guezam[3], Abdelmalek Cheknane[1], Moussa Attia[4]

[1] Electrical Engineering Department, Semi-conductors and Functional Materials Laboratory, Amar Telidji University, Laghouat 03000, Algeria
[2] Electrical Engineering Department, LeDMaScD Laboratory, Amar Telidji University, Laghouat 03000, Algeria
[3] Electrical Engineering Department, LACoSERE Laboratory, Amar Telidji University, Laghouat 03000, Algeria
[4] Environmental Laboratory, Institute of Mines, Echahid Cheikh Larbi Tebessi University, Tebessa 12002, Algeria

Corresponding Author Email: h.sayaf.elt@lagh-univ.dz

https://doi.org/10.18280/jesa.590613

Received: 22 April 2026
Revised: 19 June 2026
Accepted: 27 June 2026
Available online: 30 June 2026

Keywords:
closed-form predictive control, electric vehicle, Lyapunov stability, permanent magnet synchronous motor, ramp disturbance rejection, synergetic control

ABSTRACT

This paper combines a double integral synergetic controller (DISC) for the speed loop with a closed-form predictive current controller (derived from a short-horizon quadratic cost) for permanent magnet synchronous motor (PMSM) drives. Adding a second error integral to the synergetic manifold raises the closed-loop disturbance-rejection order from one to two, so that ramp-shaped load disturbances—as occur during gradual hill climbing or wind gusts in electric vehicle drivetrains—are rejected with zero steady-state speed error and without any disturbance observer. The inner q-axis current loop is solved analytically as a single dot product per sampling instant, with no online optimisation, while a proportional-integral (PI) controller keeps the d-axis current at zero. Lyapunov analysis confirms manifold convergence, and Routh–Hurwitz conditions on the manifold characteristic polynomial guarantee asymptotic stability of the on-manifold error dynamics. In MATLAB simulations using an averaged-inverter model, DISC reduces speed overshoot by 96% relative to integral backstepping (IBS), cuts the load-induced speed drop by 77%, recovers from disturbances about 1.7 times faster, and drives the ramp tracking error to zero. These improvements hold under +50% inertia mismatch, −25% flux variation, sinusoidal load profiles, and extreme parameter uncertainty. All reported results are simulation-based; experimental validation is left for future work.

1. INTRODUCTION

Permanent magnet synchronous motors (PMSMs) sit at the heart of most modern electric vehicle (EV) drivetrains, chosen for their high torque density and efficiency across a wide speed range [1, 2]. Controlling the speed of these motors under real driving conditions is harder than it sounds: the load torque swings continuously as the vehicle accelerates, brakes, climbs hills, or encounters crosswinds. A controller that works well on a flat road may falter when the load changes gradually rather than abruptly. The proportional-integral (PI) controller remains the workhorse of industrial drives, but its linear structure limits what it can achieve on a nonlinear plant. Parameter drifts due to temperature or aging degrade its performance, and it has no built-in mechanism for anticipating time-varying loads [3]. Over the past decade, researchers have explored a range of alternatives. Sliding mode control (SMC) delivers strong robustness at the price of chattering [4-6]. Active disturbance rejection control (ADRC) bundles all uncertainties into a single estimated disturbance and cancels them feedforward [7-9], but the observer bandwidth becomes a sensitive knob. Model predictive control (MPC) optimises the voltage over a prediction horizon [10-13], trading computational cost for fast transient response. Backstepping builds the control law recursively through Lyapunov functions [14, 15], and its integral variant eliminates steady-state offset under constant loads [16-18]. A recent study by Melkia et al. [19] applied classical backstepping (without integral action) to PMSM speed control and reported a 45% settling-time reduction relative to PI, confirming the merit of Lyapunov-based design but leaving the ramp disturbance problem unaddressed. Synergetic control, formalised by Kolesnikov [20], belongs to the same Lyapunov family but replaces the discontinuous switching surface of SMC with a smooth first-order convergence law. The result is a chattering-free controller whose robustness comes from manifold design rather than high-frequency switching. Several groups have applied synergetic control to PMSM drives. Moati and Kouzi [21] combined it with direct torque control on a matrix converter-fed dual stator machine. Boumegouas et al. [22] designed a synergetic speed observer for sensorless EV operation and a robust synergetic scheme with an improved load-torque observer for EV drives [23]. Nicola and Nicola [24] paired fractional-order synergetic control with sliding mode for PMSM position tracking. Boumegouas and Kouzi [25] proposed a six-phase synergetic EV drive scheme. Belouahchi and Merabet [26] applied the approach to direct torque control of a double-star induction motor. The question this paper addresses is whether a second integral in the manifold can eliminate that offset. From a classical control standpoint, one extra integrator in the loop raises the system type by one, granting rejection of one additional order of polynomial disturbance. The same logic applies inside the synergetic framework: a manifold built from the speed error and its first and second integrals contains two zeros at the origin in its disturbance sensitivity function, which is exactly what is needed to reject a ramp. To the best of our knowledge, double-integral synergetic manifolds have not been reported for PMSM speed control, although the underlying idea—raising the loop type by adding an integral—is well established in classical control [3]. The structure differs from integral backstepping (IBS) and integral synergetic control, which embed a single integral and remain Type-1 under a ramp; from ADRC/ESO (extended state observer), which estimates and cancels the disturbance through an observer rather than embedding integral action in a manifold; from MPC, which achieves offset-free tracking through an explicit disturbance model and online optimisation; and from higher-order sliding-mode control, which suppresses disturbances through discontinuous switching at the cost of chattering. The double integral synergetic controller (DISC) instead obtains ramp rejection structurally, from the manifold itself, without an observer, disturbance model, or switching term. The contributions are as follows. First, a DISC speed controller whose manifold embeds two error integrals achieves asymptotic ramp rejection without observers or estimators. Second, a closed-form predictive current control (PCC) inner loop with a prediction horizon of three solves the optimisation analytically, paired with a standard PI d-axis controller identical across all compared methods. Third, validation across several operating scenarios—step response, load and ramp disturbance rejection, sinusoidal load, parametric robustness, speed reversal, low-speed operation, current quality, and thermal drift with systematic comparison against PI-based field-oriented control (PI-FOC) and IBS on the same simulation platform.

2. PERMANENT MAGNET SYNCHRONOUS MOTOR MODEL AND CONTROLLER DESIGN

2.1 Permanent magnet synchronous motor mathematical model

The surface-mounted PMSM is modelled in the d–q synchronous reference frame under the standard assumptions: linear magnetic circuit, sinusoidal spatial distribution of the stator magnetomotive force (MMF), negligible eddy-current and hysteresis losses, no damper windings, uniformly magnetised permanent magnets, and a uniform air gap [1, 15]. These conditions are satisfied for high-performance servo drives operating below magnetic saturation, and they allow the Park transformation to map the three-phase machine onto two orthogonal axes with time-invariant inductances. Under these assumptions, the stator voltage equations are:

$$v_d = R_s\, i_d + L_s\,\frac{di_d}{dt} - p\,\omega_r\, L_s\, i_q \tag{1}$$

$$v_q = R_s\, i_q + L_s\,\frac{di_q}{dt} + p\,\omega_r\, L_s\, i_d + p\,\omega_r\,\psi_f \tag{2}$$

where, v_d, v_q are the d–q stator voltages [V]; i_d, i_q are the corresponding currents [A]; R_s is the stator resistance [Ω]; $L_s = L_d = L_q$ is the stator inductance [H] (the surface-mounted topology eliminates magnetic anisotropy); ω_r is the mechanical angular velocity [rad/s]; p is the number of pole pairs; and ψ_f is the permanent-magnet flux linkage [Wb]. The cross-coupling terms represent the rotational back-electromotive force (EMF) that the controller must compensate; the term $p\cdot\omega_r\cdot\psi_f$ is the back-EMF generated by the rotating magnets.

The electromagnetic torque follows from the d–q current and the flux linkage. Because the surface-mounted topology imposes equal inductances on the two axes, the reluctance term vanishes and torque becomes proportional to the q-axis current alone:

$$T_{em} = K_t\, i_q, \qquad K_t = 3p/2\;\psi_f \tag{3}$$

The rotor mechanical dynamics follow from Newton's second law:

$$J\,\frac{d\omega_r}{dt} = K_t\, i_q - T_L - B_v\,\omega_r \tag{4}$$

where, J is the rotor inertia [kg·m²], B_v is the viscous friction coefficient [N·m·s/rad], and T_L is the load torque [N·m]. Eq. (4) is the plant seen by the speed controller, with i_q as the manipulated input. The motor parameters used throughout the paper are listed in Table 1.

Table 1. Permanent magnet synchronous motor (PMSM) parameters

Parameter	Symbol	Value	Unit
Rated power	P_n	1.2	kW
Pole pairs	p	4	—
Stator resistance	R_s	0.958	Ω
Stator inductance	L_s	5.25	mH
PM flux linkage	ψ_f	0.1827	Wb
Rotor inertia	J	1.78×10^{-3}	kg·m²
Viscous friction	B_v	3.24×10^{-4}	N·m·s/rad
DC bus voltage	V_{dc}	311	V
Torque constant	K_t	1.0962	N·m/A
Control period	T_s	100	μs

2.2 Control architecture overview

The proposed scheme uses a cascaded structure: a slow outer speed loop based on the proposed DISC generates the q-axis current reference, which is tracked by a fast inner current loop based on the PCC scheme; the d-axis current is held at zero by a conventional PI controller. The cascade is justified by singular-perturbation theory [27] because the electrical time constant $\tau_e = L_s/R_s = 5.48$ ms is roughly three orders of magnitude smaller than the mechanical time constant $\tau_m = J/B_v = 5.49$ s. This separation lets the speed-loop design treat $i_q \approx i_q^*$ without modelling the inner current dynamics explicitly. The complete control law is derived below.

2.3 Double integral synergetic controller

Synergetic control [20] selects a smooth macro-variable

$\psi(x)$ of the system states and forces it to obey a first-order convergence law:

$$T\,\frac{d\psi}{dt} + \psi = 0, \qquad T > 0 \tag{5}$$

For the speed loop, three error states are defined: the speed error itself, its first integral, and its second integral.

$$z_\omega = \omega_{rf} - \omega_r, z_{\omega i} = \int z_\omega \, d\tau, z_{\omega ii} = \int z_{\omega i} \, d\tau \tag{6}$$

The macro-variable is then a linear combination of all three:

$$\psi = k_\omega \, z_\omega + k_{\omega i} \, z_{\omega i} + k_{\omega ii} \, z_{\omega ii} \tag{7}$$

The control law is obtained by differentiating Eq. (7) with respect to time, substituting the mechanical model Eq. (4), and enforcing the convergence law Eq. (5). The first term in $d\psi/dt$ contains $dz_\omega/dt = d\omega_{rf}/dt - d\omega_r/dt$, and $d\omega_r/dt$ is given by Eq. (4).

$$i_q^* = \frac{J}{K_t}\left[\dot{\omega}_{rf} + \frac{B_v}{J}\,\omega_r + \frac{1}{k_\omega}\left(k_{\omega i}\, z_\omega + k_{\omega ii}\, z_{\omega i} + \frac{\psi}{T}\right)\right] \tag{8}$$

The load torque T_L does not appear in Eq. (8)—it is unknown to the controller, and the integral states $z_{\omega i}$ and $z_{\omega ii}$ are precisely what compensate for it. Under a constant load, $z_{\omega i}$ ramps up until $k_{\omega i} \cdot z_\omega$ cancels the disturbance term, leaving a Type-1 servo behaviour. Under a ramp load $T_L = R \cdot t$, a single integrator can no longer follow the disturbance, and a Type-1 controller settles at a non-zero offset; the second integral $z_{\omega ii}$ integrates the residual offset, eventually driving it to zero. This is what raises the closed-loop type from one to two; the formal proof is given in Section 2.6.

The convergence parameter T in Eq. (5) is made error-dependent:

$$T(e_\omega) = T_{\max} - (T_{\max} - T_{\min})\exp\left(-\alpha\,|e_\omega|\right) \tag{9}$$

This form gives a small T near steady state (tight regulation, ψ converges quickly) and a larger T during large transients (gentle convergence, smaller spikes in i_q^*). The constants T_{min}, T_{max} and α are listed in Table 2.

2.4 Closed-form predictive current controller

Once the cross-coupling terms in Eqs. (1) and (2) are compensated by feedforward, the q-axis current dynamics reduce to a first-order linear equation.

Discretising by forward Euler at sampling period T_s gives $i_q(k + 1) = A_d \cdot i_q(k) + B_d \cdot v_q'(k)$, with $A_d = 1 - R_s \cdot T_s/L_s = 0.98175$ and $B_d = T_s/L_s = 1.905 \times 10^{-2}$. The Euler step is justified by $R_s \cdot T_s/L_s = 0.0183 \ll 1$; A_d differs from the exact value $\exp(-R_s \cdot T_s/L_s) = 0.98192$ by less than 0.02%.

Over a prediction horizon of $N_p = 3$ with constant control across the horizon, the predicted current vector is $\hat{I}_q = F \cdot i_q(k) + G \cdot v_q'$ with $F = [A_d, A_d^2, A_d^3]^T$ and $G_j = (1 + A_d + \cdots + A_d^{j-1}) \cdot B_d$. The cost function (based on a prediction horizon of $N_p = 3$) penalises tracking error and control effort:

$$J_{MPC} = \| I_q^* - \hat{I}_q \|^2 + \lambda_u \left(v_q'\right)^2 \tag{10}$$

Setting $dJ_{MPC}/dv_q' = 0$ yields the unconstrained optimum v_q' opt $= (G^TG + \lambda_u)^{-1} \cdot G^T \cdot (I_q^* - F \cdot i_q(k))$. To suppress steady-state offsets caused by parameter mismatch, an integral feedforward term $K_i \cdot e_{int}$ is added, giving the implemented control law:

$$v_q'^{*} = (G^\top G + \lambda_u)^{-1}\left[G^\top(I_q^* - F\, i_q(k)) + K_i\, e_{int}\right] \tag{11}$$

Because $(G^\top G + \lambda_u)$ is a scalar, the closed-form predictive control law (11) collapses to a single dot product per sampling instant—about twelve floating-point operations, well within the budget of a low-end digital signal processor (DSP). The d-axis current is held at zero by a PI controller with $K_p = 33$, $K_i = 6020$, identical for all controllers under comparison.

The resulting voltage commands are applied through an averaged inverter representation, with the linear-modulation amplitude limit $V_{max} = V_{dc}/\sqrt{3} \approx 179.6$ V enforced as a saturation on $\sqrt{v_d^2 + v_q^2}$. Table 2 lists the controller parameters of DISC and the IBS baseline.

Table 2. Controller parameters

Parameter	IBS	DISC	Stability Condition
k_ω	80	30	$k_\omega > 0$
$k_{\omega i}$	350	1000	$k_{\omega i} > 0$
$k_{\omega ii}$	—	2144	$k_{\omega ii} > 0$
T (convergence) ms	—	adaptive	$T > 0$
T_{min} / T_{max} ms	—	0.2 / 2.5	—
α (adaptation) s/rad	—	0.08	—
α_{iq} (filter)	0.65	0.41	$0 < \alpha < 1$
MPC: N_p / λ_u / K_i	—	3 / 5×10^{-4} / 200	—

Note: IBS = integral backstepping; DISC = double integral synergetic controller; MPC = Model predictive control.

2.5 d-axis current control with voltage limitation

The d-axis current is regulated to zero by a conventional PI controller with proportional gain $K_{pd} = 33$ and integral gain $K_{id} = 6020$, identical for all controllers under comparison. These gains are obtained by pole placement of the d-axis closed-loop transfer function at a bandwidth $\omega_{cd} \approx 6300$ rad/s, which is approximately one decade above the speed-loop bandwidth and preserves the singular-perturbation separation that justifies the cascade design. The combined voltage command (v_d, v_q) produced by the d-axis PI and the q-axis predictive controller is applied through an averaged inverter representation. To ensure operation within the linear modulation region of the inverter, the magnitude $\sqrt{v_d^2 + v_q^2}$ is constrained to $V_{max} = V_{dc}/\sqrt{3} \approx 179.6$ V; when this limit is reached, both components are scaled proportionally so that the voltage vector remains on the saturation circle while preserving its direction. No active anti-windup is needed for the d-axis loop because $i_d^* = 0$ and the d-axis controller does not drive the saturation; the q-axis integral term is bounded by the clamp described in Section 2.4.

2.6 Stability analysis and asymptotic ramp rejection

Consider the Lyapunov candidate $V = \psi^2/2$. Its time derivative along the convergence law Eq. (5) is $dV/dt = \psi \cdot d\psi/dt = -\psi^2/T < 0$ for all $\psi \neq 0$, establishing Lyapunov stability of the manifold dynamics and exponential convergence of ψ to zero with time constant T. On the manifold ($\psi = 0$), substituting Eq. (7) and differentiating twice yields the linear error dynamics $k_\omega \cdot \ddot{z}_\omega + k_{\omega i} \cdot \dot{z}_\omega + k_{\omega ii} \cdot z_\omega = 0$, with characteristic polynomial:

$$k_\omega s^2 + k_{\omega i} s + k_{\omega ii} = 0 \tag{12}$$

Routh–Hurwitz stability requires k_ω, $k_{\omega i}$, $k_{\omega ii} > 0$ (coefficients of one sign), which is sufficient and easy to enforce. For the values in Table 2, $30s^2 + 1000s + 2144$ has real roots $s_1 \approx -2.30$ and $s_2 \approx -31.03$, so the system is overdamped and the slower mode dominates the load-rejection envelope.

Gain selection methodology. Pole placement gives $k_{\omega i}/k_\omega = |s_1| + |s_2|$ and $k_{\omega ii}/k_\omega = |s_1| \cdot |s_2|$. With the chosen poles and $k_\omega = 30$, this yields $k_{\omega i} = 1000$ and $k_{\omega ii} = 2144$. The gains in Table 2 thus follow directly from the desired pole placement rather than from empirical tuning.

For fairness of comparison, the IBS gains in Table 2 ($k_\omega = 80$, $k_{\omega i} = 350$) are not retuned here: they are the values originally reported for the same motor and operating point in the integral-backstepping baseline of the authors' prior work, where they were obtained by pole placement on the IBS Lyapunov-derived characteristic polynomial with a settling-time target matched to the same reference bandwidth ($\omega_n = 120$ rad/s, $\zeta = 0.85$) used in the present study. Carrying these gains forward unchanged keeps the IBS baseline directly comparable across the authors' paper family and removes the risk of an opportunistic retuning that would bias the IBS-vs-DISC comparison. The PI-FOC speed-loop gains used in the simulation comparison (Section 3) are likewise derived analytically from J, B_v and K_t for the same reference bandwidth used by DISC, so that all three speed controllers receive comparable tuning effort. To make this claim explicit, the disturbance sensitivity transfer function $S_d(s)$ is now written out for both controllers under the standard assumptions: (i) the inner current loop tracks instantly, so that $i_q \approx i_q^*$, reducing the speed plant to:

$$J\frac{d\omega}{dt} = K_t\, i_q^* - T_L - B_v\, \omega_r \tag{13}$$

with i_q^* given by the speed-loop control law; (ii) neither the voltage nor the current saturates, so the linear analysis applies; (iii) the d-axis current is regulated to zero and decoupled, and so does not enter the speed dynamics; (iv) the reference filter has reached steady state for the disturbance-response derivation. Defining the speed error as:

$$e_\omega = \omega_{rf} - \omega \tag{14}$$

Substituting the IBS law [16, 17] into the plant and solving in the Laplace domain gives:

$$S_d^{IBS}(\mathrm{s}) = \frac{s}{J\,[\,s^2 + (k_\omega + k_{\omega i})s + k_\omega k_{\omega i}]} \tag{15}$$

which has a single zero at s = 0. Substituting the DISC law of Eq. (8) in Section 2.3 (with the convergence parameter T held at its nominal value for this linear analysis) into the plant and solving for e_ω yields:

$$S_d^{DISC}(\mathrm{s}) = \frac{T\, k_\omega s^2}{J[T\, k_\omega s^3 + (T\, k_{\omega i} + k_\omega)s^2 + (T\, k_{\omega ii} + k_{\omega i})s + k_{\omega ii}]} \tag{16}$$

which has a double zero at s = 0. The structural reason is that the IBS manifold contains one integral of the speed error, so its Laplace expression carries one factor of 1/s, which closes through the loop into one s in the numerator of $S_d(s)$; the DISC manifold contains two integrals (the first and the second integral of the speed error), so the closed-loop disturbance sensitivity carries an s^2 factor in the numerator. Under a ramp $T_L = R \cdot t$ with Laplace transform R/s^2, the final value theorem gives:

$$e_{ss}^{IBS} = \lim_{s\to 0} s \cdot S_d(s) \cdot \frac{R}{s^2} = \frac{R}{J\, k_\omega\, k_{\omega i}} \tag{17}$$

$$e_{ss}^{DISC} = \lim_{s\to 0} s \cdot S_d(s) \cdot \frac{R}{s^2} = 0 \tag{18}$$

For R = 1.5 N·m/s and the IBS gains in Table 2, e_{ss}^{IBS}= $1.5/(1.78 \times 10^{-3} \cdot 80 \cdot 350) = 0.0301$ rad/s, matching the ramp-load simulation of Section 3.3 to four significant figures. Doubling the slope to R = 3.0 N·m/s gives $e_{ss}^{IBS} = 0.0602$ rad/s, also confirmed by simulation. DISC drives the error to zero in both cases.

Counting rule. The closed-loop type equals the number of zeros of $S_d(s)$ at s = 0 [28]: Type-0 leaves a step offset, Type-1 rejects steps but leaves a ramp offset, Type-2 rejects both. A parabolic disturbance $T_L = R \cdot t^2/2$ would still leave a finite error, requiring a third integrator. The proposed DISC therefore covers the two most common load profiles in EV traction—constant cruise and gradual hill—without disturbance estimation.

3. SIMULATION RESULTS

All simulations use the PMSM parameters of Table 1 with an average-model voltage-source inverter, solved in MATLAB at $T_s = 100$ µs. The three controllers —IBS, PI-FOC, and the proposed DISC — share the same d-axis PI current regulator and the same second-order reference filter ($\omega_n = 150$ rad/s, $\zeta = 0.95$), so the comparison isolates the speed-loop structure. The PI-FOC speed-loop gains are obtained analytically by pole placement as $K_p = (2\zeta\omega_n J - B_v)/K_t = 0.4625$ and $K_i = (\omega_n^2 J)/K_t = 36.54$, using the same reference bandwidth as DISC. The validation covers several scenarios: step response, load-disturbance rejection, ramp-load tracking, sinusoidal load disturbance, parametric robustness, speed reversal, low-speed operation, current quality, and combined thermal drift. These span the characteristic operating events of an electric-vehicle drive — tip-in acceleration, constant cruise, gradually rising hill-climb torque, periodic road undulation, payload and magnet-heating parameter changes, and aggressive reversal.

To ensure reproducibility, Table 3 summarises the MATLAB version, the numerical solver, the sampling and integration steps, the averaged-inverter model, the voltage and current saturation handling, the reference-filter parameters, and the load-disturbance schedules used across all scenarios.

3.1 Step response

A 100 rad/s speed step is applied at t = 0.02 s with no load. All three controllers reach the reference within 35–40 ms (Figure 1(a)). The zoom (Figure 1(b)) shows the difference in damping: PI-FOC overshoots by 4.00%, IBS by 0.57%, while

DISC rises monotonically with a negligible 0.025% overshoot. The double integral therefore adds the rejection order without the overshoot penalty usually associated with extra integral action.

Table 3. Simulation settings (reproducibility)

Item	Value
MATLAB version	R2023a (script-based)
Numerical solver	Forward Euler (fixed-step)
Plant integration step T_s	10 µs
Controller sampling period $T_{s,ctrl}$	100 µs (control loop runs every 10th plant step)
Inverter model	Averaged: v_d, v_q applied directly; no pulse-width modulation (PWM), no dead-time, no switching ripple
Voltage saturation	$\sqrt{(v_d^2+v_q^2)}$ clamped to $V_{max} = V_{dc}/\sqrt{3} \approx$ 179.6 V; direction preserved
Current saturation	$\lvert i_q^*\rvert$ clamped to I_{max} = 18.9 A
Reference filter	2nd-order, ω_n = 150 rad/s, ζ = 0.95 (DISC, PI-FOC); ω_n = 120 rad/s, ζ = 0.85 (IBS)
Step reference	ω^* = 100 rad/s applied at t = 0.02 s
Constant load	T_L = 5 N·m applied at t = 0.4 s
Ramp load	$T_L = R\cdot(t - 0.5)$ with R = 1.5 N·m/s, applied at t = 0.5 s
Sinusoidal load	$T_L = 3 + 3\cdot\sin(10\pi\ t)$ N·m (applied at t = 0.4 s)
Parametric robustness	Nominal: J × 1.5, ψ_f × 0.75, L × 1.2, R_s × 1.3; Thermal drift: R_s × 1.5, L × 1.2, ψ_f × 0.85 (Section 3.5)
Simulation horizon	2 s (4 s for ramp tests)

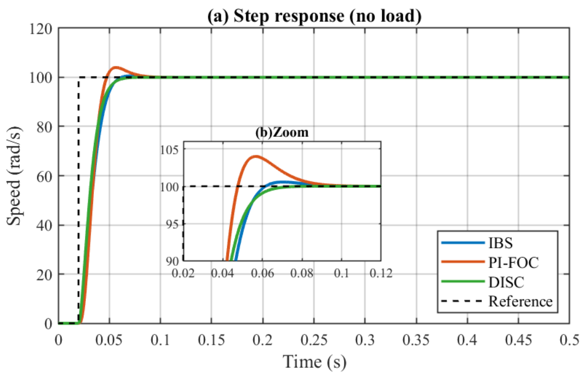

Figure 1. Step response: (a) speed, (b) zoom

3.2 Load disturbance rejection

A 5 N·m load step is applied at t = 0.4 s at 100 rad/s. The error transient (Figure 2) separates the three controllers clearly: the peak speed dip is 7.31 rad/s for PI-FOC, 5.73 rad/s for IBS, and only 1.29 rad/s for DISC. DISC also recovers fastest, settling within the ±5% band in 39.6 ms, against 48.4 ms for PI-FOC and 67.2 ms for IBS. The second manifold integral cancels the constant load far more aggressively than the single integral of IBS or the linear PI action.

3.3 Ramp-load and sinusoidal disturbances

A ramp load TL = R·t with R = 1.5 N·m/s is applied from t = 0.5 s. This is the decisive test (Figure 3): IBS settles to a finite steady-state error of 0.030 rad/s and PI-FOC to 0.038 rad/s — both Type-1 against the ramp — whereas DISC drives the error through a small transient (peak ≈ 0.004 rad/s) back toward zero (≈ 0.0006 rad/s), confirming Type-2 behaviour. The measured IBS value matches the closed-form prediction $R/(J\cdot k_\omega\cdot k_{\omega i})$ = 0.0301 rad/s of Section 2.6.

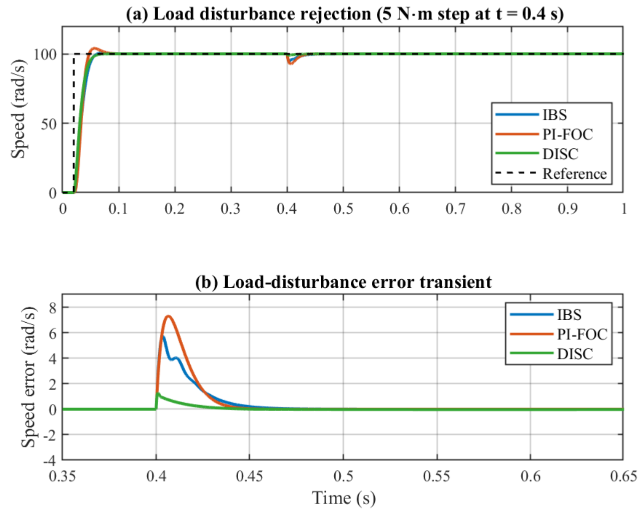

Figure 2. Load disturbance: (a) speed, (b) error transient

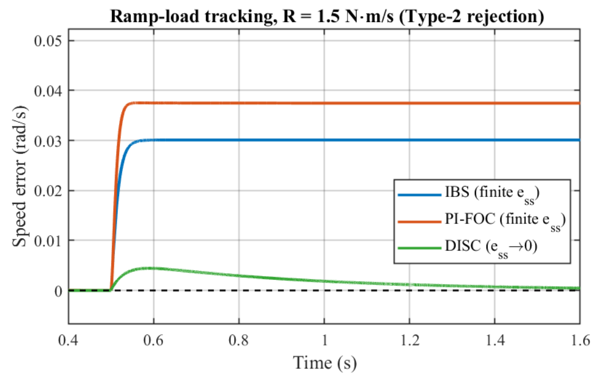

Figure 3. Ramp-load tracking (R = 1.5 N·m/s): speed error showing Type-2 rejection

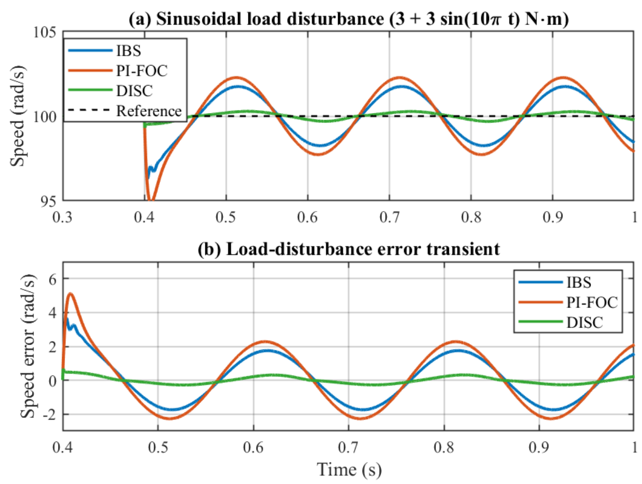

Figure 4. (a) Sinusoidal load disturbance, (b) error

A periodic load $T_L = 3 + 3\sin(10\pi\ t)$ N·m is then applied from t = 0.4 s. Under this 5 Hz disturbance (Figure 4(a)), the speed of IBS and PI-FOC swings by about ±2 rad/s, while DISC holds within roughly ±0.3 rad/s. The error subplot (Figure 4(b)) shows DISC attenuating the periodic component by a factor of six to seven relative to the two baselines, a direct consequence of the higher loop type.

3.4 Robustness and operating-range tests

The combined mismatch J × 1.5, ψ_f × 0.75, L × 1.2, R_s × 1.3 is applied together with the 5 N·m load (Figure 5). PI-FOC is the most sensitive, with its overshoot growing to about 13% and its load dip to roughly 8.5 rad/s, while IBS overshoots about 3% with a dip near 6.3 rad/s. DISC remains close to its nominal behaviour, with overshoot under 1% and a load dip of about 1.8 rad/s, confirming that the manifold-based design does not rely on accurate parameters.

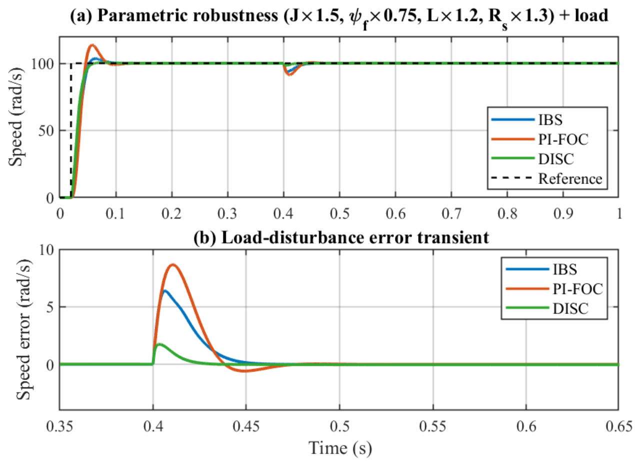

Figure 5. Parametric robustness (J × 1.5, ψ_f × 0.75, L × 1.2, R_s × 1.3) with load: (a) speed, (b) error transient

A symmetric +100 → −100 rad/s reversal at t = 0.5 s is commanded with a 3 N·m load from t = 0.2 s (Figure 6). All three controllers follow the reversal without instability; PI-FOC shows a small overshoot at the load step and a slight undershoot at the reversal, whereas IBS and DISC track the command cleanly. The test confirms correct four-quadrant operation.

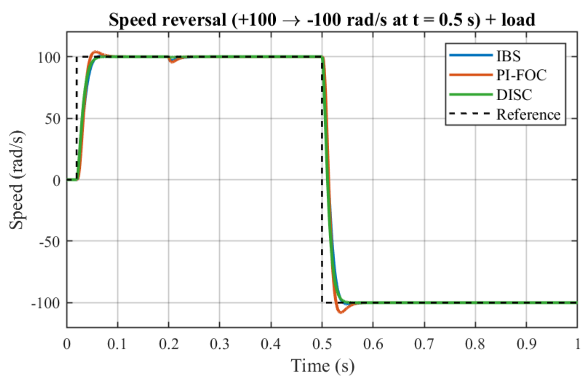

Figure 6. Speed reversal (+100 → −100 rad/s at t = 0.5 s) with load

At a low reference ω* = 10 rad/s with a 2 N·m load at t = 0.4 s (Figure 7), the load dip is largest for PI-FOC (down to ≈ 7 rad/s), smaller for IBS, and smallest for DISC; all three recover to the reference. DISC therefore keeps its disturbance-rejection advantage in the low-speed region where back-EMF is small, and regulation is harder.

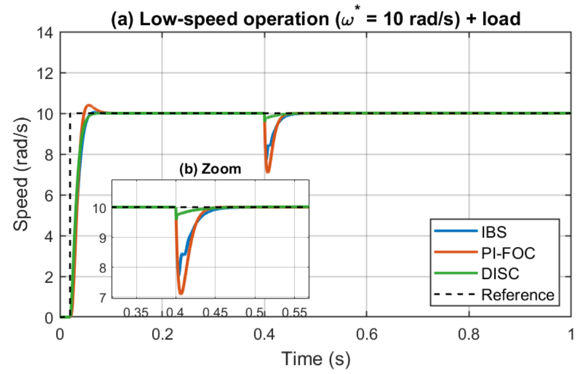

Figure 7. Low-speed operation (ω* = 10 rad/s) with load: (a) speed, (b) zoom

3.5 Current quality and thermal drift

Because the d-axis loop is common to the three controllers, a single representative run (DISC) is shown in Figure 8. The d-axis current is held at i_d ≈ 0 throughout, so the surface-mounted machine operates on its maximum-torque-per-ampere (MTPA) line; the q-axis current rises to about 4.6 A under the 5 N·m load with a brief ≈ 9 A start-up transient. The stator-voltage magnitude (Figure 8, bottom) settles near 77 V, well below the space vector modulation (SVM) limit V_{max} = $V_{dc}/\sqrt{3}$ = 179.6 V, so no voltage saturation occurs, and the linear analysis of Section 2 applies.

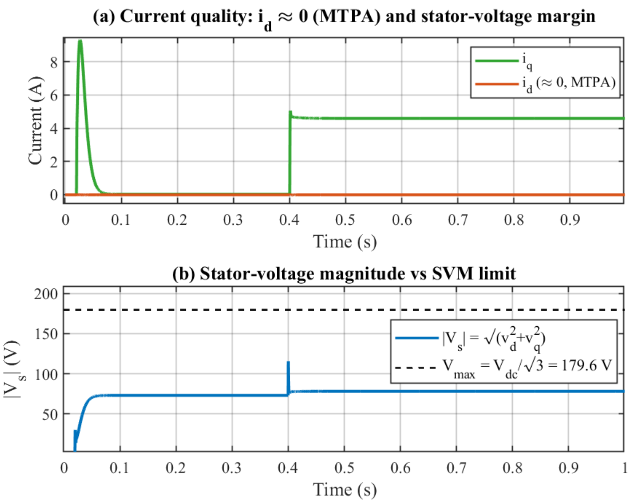

Figure 8. Current quality and MTPA (DISC): (a) dq currents with i_d ≈ 0, (b) stator-voltage magnitude versus the SVM limit

Note: maximum-torque-per-ampere (MTPA); space vector modulation (SVM).

Finally, sustained heating is emulated by R_s +50%, L +20%, ψ_f −15% with the 5 N·m load (Figure 9). PI-FOC overshoot rises to 6.00% and its load dip to 8.59 rad/s, IBS to 0.83% and 6.89 rad/s, while DISC stays at 0.03% overshoot and a 1.64 rad/s dip — essentially its nominal performance. The double integral absorbs the slow parameter drift without any thermal model or observer.

3.6 Performance summary

Table 4 reports the quantitative gains for the canonical step-plus-load test. Across all tested scenarios, DISC consistently improves overshoot, load drop, recovery time, and the integral error indicators, while remaining comparable to IBS on settling and rise time. Relative to IBS, DISC reduces overshoot by about 96%, the load-induced dip by about 77%, recovers roughly 1.7 times faster, and lowers the integral of the time-weighted absolute error (ITAE) by about 34%; the same ordering holds under thermal drift. The integral error indicators reported in Table 4 are the integral of the absolute error (IAE), the integral of the squared error (ISE), ITAE, and the root-mean-square error (RMS).

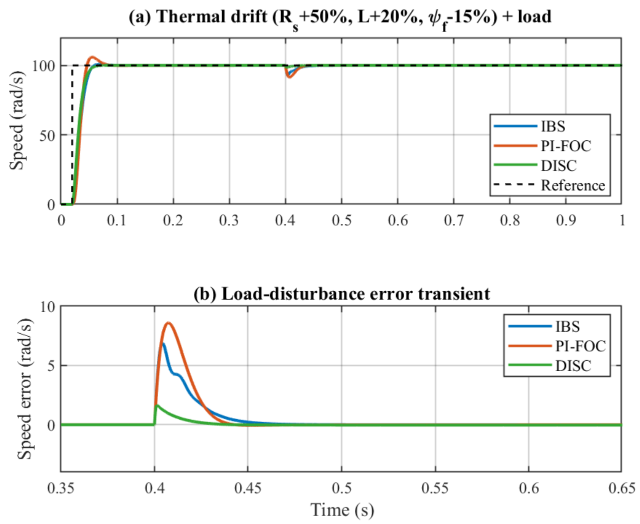

Figure 9. Thermal drift (R_s +50%, L +20%, ψ_f −15%) with load: (a) speed, (b) error transient

Because all three controllers use the identical predictive current loop, any difference among them is attributable to the speed-loop structure (PI vs IBS vs DISC). The DISC speed loop therefore accounts for the gains reported on overshoot, load drop, ramp tracking, and the integral error indicators. A separate cross-ablation pairing DISC with a PI current loop and IBS with the predictive current loop would, by the same logic, isolate the inner-loop effect; given that the q-axis dynamics are first-order with an electrical time constant much smaller than the speed loop, the inner-loop contribution is expected to be small for the metrics considered here and is the subject of a follow-up study.

Table 4. Quantitative comparison (step + load scenario), single consistent simulation engine

Metric	IBS	PI-FOC	DISC	Improvement
Overshoot (%)	0.57	4.00	0.025	96%
Load drop (rad/s)	5.73	7.31	1.29	77%
Recovery time (ms)	67	48	40	1.7×
Settling time (ms)	31	44	32	≈ equal
Ramp e_{ss} (rad/s)	0.030	—	≈ 0	≫
IAE	1.53	1.56	1.29	16%
ISE	94.4	100.6	79.6	16%
ITAE	0.085	0.095	0.056	34%
RMS (rad/s)	6.87	7.09	6.31	8%

Note: IBS = integral backstepping; PI-FOC = PI-based field-oriented control; DISC = double integral synergetic controller; IAE = integral of the absolute error; ISE = integral of the squared error; ITAE = integral of the time-weighted absolute error; RMS = root-mean-square error; e_{ss} = steady-state error.

4. COMPARISON WITH LITERATURE

Table 5 positions DISC against representative PMSM speed-control methods reported in the literature. Because the cited works use different motors, loads, samplings and benchmark scenarios, the numerical columns of Table 5 are intended as qualitative indicators only; the structural columns (servo type, observer use, experimental status) carry the bulk of the comparison.

Table 5. Positioning against recent permanent magnet synchronous motor (PMSM) control methods

Method	Type	OS%	Drop	Ts (ms)	Ramp e_ss	Obs	Ref.
PI-FOC	1	3–5	high	50–80	≠0	no	[3]
SMC	1	<1	med.	30-50	≠0	yes	[4, 5]
ADRC/ESO	1	<2	low	30–50	≠0	yes	[6, 7]
Backstepping	0	~0	med.	10–15	≠0	no	[15]
IBS	1	0.57	5.73	35	≠0	no	[13]
FO-SC + SMC	1	~1.5	~5	~80	≠0	no	[19]
SC + DTC (MC)	1	~2	19	87	≠0	no	[17]
SynO (EV)	1	—	—	—	—	yes	[18]
DISC (this work)	2	0.025	1.29	32	≈0	no	—

Note: PI-FOC = PI-based field-oriented control; SMC = sliding mode control; ADRC/ESO = active disturbance rejection control/extended state observer; IBS = integral backstepping; FO-SC + SMC = fractional-order synergetic control combined with sliding mode control; SC + DTC (MC) = synergetic control with direct torque control on a matrix converter; SynO (EV) = synergetic observer (electric vehicle); DISC = double integral synergetic controller; Type = closed-loop system type; OS = overshoot; T_s = settling time; e_{ss} = ramp steady-state error; Obs = disturbance observer required.

The asymptotic ramp rejection is the distinguishing feature: no controller in Table 5 achieves zero ramp error without a disturbance observer.

5. CONCLUSIONS

Augmenting the synergetic manifold with a second integral entails negligible computational overhead (one additional accumulator per sampling period) while fundamentally upgrading disturbance rejection from constant-load to ramp-load, a qualitative change that no amount of gain tuning can achieve in a single-integral controller. The ramp tracking error drops from 0.030 rad/s (IBS, matching the theoretical Type-1 limit) to effectively zero (DISC), confirmed both by the closed-form derivation of Section 2.6 and by simulation at two ramp rates. Across the tested scenarios — step, load, ramp, sinusoidal load, parametric robustness, speed reversal, low-speed operation and thermal drift — DISC consistently outperforms the IBS baseline: 96% less overshoot, 77% less load drop, about 1.7 times faster recovery, and robust performance under +50% inertia, −25% flux, +20% inductance and +30% resistance variation. The closed-form predictive current controller (inner loop) contributes faster current tracking through its analytical closed-form solution. The present study is a simulation study, limited to an averaged-inverter model under the scenarios described in Section 3. It does not include switching-harmonic analysis, sensor noise, a coupled electrothermal model, or a real electric-vehicle driving cycle, and no experimental validation has been performed; the reported gains should be read accordingly. Extending the approach to a real PWM inverter with switching harmonics and incorporating quasi-resonant controllers for harmonic suppression is the natural next step. Experimental validation on a DSP platform is planned.

ACKNOWLEDGMENT

This work was supported by the Semi-conductors and Functional Materials Laboratory and the LACoSERE Laboratory at Amar Telidji University, Laghouat, Algeria.

REFERENCES

[1] Pillay, P., Krishnan, R. (1989). Modeling, simulation, and analysis of permanent-magnet motor drives. I. The permanent-magnet synchronous motor drive. IEEE Transactions on Industry Applications, 25(2): 265-273. https://doi.org/10.1109/28.25541

[2] Hoai, H.K., Chen, S.C., Than, H. (2020). Realization of the sensorless permanent magnet synchronous motor drive control system with an intelligent controller. Electronics, 9(2): 365. https://doi.org/10.3390/electronics9020365

[3] Lai, C.Y., Feng, G.D., Mukherjee, K., Kar, N.C. (2017). Investigations of the influence of PMSM parameter variations in optimal stator current design for torque ripple minimization. IEEE Transactions on Energy Conversion, 32(3): 1052-1062. https://doi.org/10.1109/TEC.2017.2682178

[4] Wang, Y.Q., Feng, Y.T., Zhang, X.G., Liang, J. (2020). A new reaching law for antidisturbance sliding-mode control of PMSM speed regulation system. IEEE Transactions on Power Electronics, 35(4): 4117-4126. https://doi.org/10.1109/TPEL.2019.2933613

[5] Junejo, A.K., Xu, W., Mu, C.X., Ismail, M.M., Liu, Y. (2020). Adaptive speed control of PMSM drive system based a new sliding-mode reaching law. IEEE Transactions on Power Electronics, 35(11): 12110-12121. https://doi.org/10.1109/TPEL.2020.2986893

[6] Lv, D., Zhang, C., Zhao, W.T. (2025). A robust and chattering-free control method for the speed of PMSM drive systems based on new adaptive reaching law. Electrical Engineering, 107: 13947-13958. https://doi.org/10.1007/s00202-025-03243-z

[7] Kuang, Z., Du, B.C., Cui, S.M., Chan, C.C. (2019). Speed control of load torque feedforward compensation based on linear active disturbance rejection for five-phase PMSM. IEEE Access, 7: 159787-159796. https://doi.org/10.1109/ACCESS.2019.2950368

[8] Ding, Y., Kang, E., Wang, S., Chen, G.R., Liu, F.Y. (2019). Disturbance suppression for PMSM by a non-linear composite controller based on two-channel strategy. IET Electric Power Applications, 14(1): 31-40. https://doi.org/10.1049/iet-epa.2019.0354

[9] Dahnoun, I., Bourek, A., Ammar, A., Belaroussi, O. (2024). Active disturbance rejection control based sensorless model predictive control for PMSM. Journal Européen des Systèmes Automatisés, 57(1): 117-125. https://doi.org/10.18280/jesa.570112

[10] Tang, P., Dai, Y.H., Li, Z.Y. (2019). Unified predictive current control of PMSMs with parameter uncertainty. Electronics, 8(12): 1534. https://doi.org/10.3390/electronics8121534

[11] Benhamida, I., Ameur, A., Kouzi, K., Gaoui, B. (2019). Torque ripple minimization in predictive torque control method of PMSM drive using adaptive fuzzy logic modulator and EKF estimator. Journal of Control, Automation and Electrical Systems, 30(6): 1007-1018. https://doi.org/10.1007/s40313-019-00505-7

[12] Liu, Q., Hameyer, K. (2016). Torque ripple minimization for direct torque control of PMSM with modified FCSMPC. IEEE Transactions on Industry Applications, 52(6): 4855-4864. https://doi.org/10.1109/TIA.2016.2599902

[13] Errouissi, R., Ouhrouche, M., Chen, W.H., Trzynadlowski, A.M. (2012). Robust nonlinear predictive controller for permanent-magnet synchronous motors with an optimized cost function. IEEE Transactions on Industrial Electronics, 59(7): 2849-2858. https://doi.org/10.1109/TIE.2011.2157276

[14] Sun, X.F., Yu, H.S., Yu, J.P., Liu, X.D. (2019). Design and implementation of a novel adaptive backstepping control scheme for a PMSM with unknown load torque. IET Electric Power Applications, 13(4): 445-455. https://doi.org/10.1049/iet-epa.2018.5656

[15] Krstic, M., Kanellakopoulos, I., Kokotovic, P.V. (1995). Nonlinear and Adaptive Control Design. Wiley, New York.

[16] Hamida, M.A., Glumineau, A., de Leon, J. (2012). Robust integral backstepping control for sensorless IPM synchronous motor controller. Journal of the Franklin Institute, 349(5): 1734-1757. https://doi.org/10.1016/j.jfranklin.2012.02.005

[17] Larbaoui, A., Belabbes, B., Meroufel, A., Tahour, A., Bouguenna, D. (2014). Backstepping control with integral action of PMSM integrated according to the MRAS observer. IOSR Journal of Electrical and Electronics Engineering, 9(4): 59-69. https://doi.org/10.9790/1676-09415969

[18] Djouadi, H., Ouari, K., Belkhier, Y., Lehouche, H., Bajaj, M., Blazek, V. (2024). Improved robust model predictive control for PMSM using backstepping control and incorporating integral action with experimental validation. Results in Engineering, 23: 102416. https://doi.org/10.1016/j.rineng.2024.102416

[19] Melkia, C., Attia, M., Daouadi, R., Rais, K. (2025). Improved PMSM speed control using backstepping: Stability and performance analysis. Journal Européen des Systèmes Automatisés, 58(2): 383-392. https://doi.org/10.18280/jesa.580219

[20] Kolesnikov, A.A. (2014). Introduction of synergetic control. In 2014 American Control Conference, Portland, OR, USA, pp. 3013-3016. https://doi.org/10.1109/ACC.2014.6859397

[21] Moati, Y., Kouzi, K. (2020). Direct torque control of

indirect three-level matrix converter fed dual stator induction machine based on synergetic controller. Journal Européen des Systèmes Automatisés, 53(5): 617-627. https://doi.org/10.18280/jesa.530504
[22] Boumegouas, M.K.B., Ilten, E., Kouzi, K., Demirtas, M., M'hamed, B. (2024). Application of a novel synergetic observer for PMSM in electrical vehicle. Electrical Engineering, 106: 5507-5521. https://doi.org/10.1007/s00202-024-02297-9
[23] Boumegouas, M.K.B., Kouzi, K., Birame, M. (2024). Robust synergetic control of electric vehicle equipped with an improved load torque observer. International Journal of Emerging Electric Power Systems, 25(2): 197-205. https://doi.org/10.1515/ijeeps-2022-0311
[24] Nicola, M., Nicola, C.I. (2020). Sensorless fractional order control of PMSM based on synergetic and sliding mode controllers. Electronics, 9(9): 1494. https://doi.org/10.3390/electronics9091494
[25] Boumegouas, M., Kouzi, K. (2022). A new synergetic scheme control of electric vehicle propelled by six-phase permanent magnet synchronous motor. Advances in Electrical and Electronic Engineering, 20(1): 1-14. https://doi.org/10.15598/aeee.v20i1.4221
[26] Belouahchi, F., Merabet, E. (2020). Design of a direct torque controller based on synergetic theory for double star induction motor. Journal Européen des Systèmes Automatisés, 53(6): 903-914. https://doi.org/10.18280/jesa.530616
[27] Khalil, H.K. (2002). Nonlinear Systems, 3rd edition. Prentice Hall, Upper Saddle River, NJ. https://flyingv.ucsd.edu/krstic/files/Khalil-3rd.pdf.
[28] Franklin, G.F., Powell, J.D., Emami-Naeini, A. (2015). Feedback Control of Dynamic Systems. 7th edition. Pearson, Upper Saddle River, NJ. https://scsolutions.com/publication/feedback-control-of-dynamic-systems-seventh-edition/.